Energy & Environmental Science

ROYAL SOCIETY OF CHEMISTRY

PAPER

View Article Online
View Journal | View Issue

Cite this: *Energy Environ. Sci.*, 2025, **18**, 3014

Tailoring zinc diatomic bidirectional catalysts achieving orbital coupling–hybridization for ultralong-cycling zinc–iodine batteries†

Chenxu Dong, ‡[a] Yongkun Yu,‡[a] Changning Ma,[a] Cheng Zhou,[a] Jiajing Wang,[a] Jiapei Gu,[a] Juan Ji,[a] Shubin Yang, [c] Zunfeng Liu, [d] Xu Xu*[ab] and Liqiang Mai*[a]

Received 6th December 2024,
Accepted 30th January 2025

DOI: 10.1039/d4ee05767h

rsc.li/ees

Aqueous zinc–iodine ($Zn–I_2$) batteries have become promising energy storage devices due to their high theoretical capacity, high safety, and low cost advantages. However, sluggish kinetics and the shuttle effect of polyiodides still limit the further development of $Zn–I_2$ batteries. Single-atom catalysts have been explored in $Zn–I_2$ batteries to address the above challenges, but single atom sites restrict the adsorption/desorption relationship of reactants and intermediates. Herein, honeycomb shaped Zn dual atom sites embedded in nitrogen doped carbon nanosheets were designed to not only enhance the confinement of I_2, but also facilitate the bidirectional redox kinetics of polyiodides through orbital coupling and hybridization, thereby improving the capacity and cycle stability of $Zn–I_2$ batteries. Impressively, the batteries with I_2@Zn_2NC cathodes received the longest cycle of 100 000 cycles at 50C, retaining an ultra-low capacity fading of 0.0002% per cycle. Additionally, the batteries achieved 7000 cycles at 10C even at −20 °C, verifying good catalytic performance of Zn_2NC at low temperature. This work reveals the mechanism of synergistic adsorption and catalytic conversion of polyiodides by dual single atom catalysts, providing guidance for the design of dual atom site structures to achieve state-of-the-art $Zn–I_2$ batteries.

Broader context

Aqueous zinc iodine batteries have attracted widespread attention due to their advantages of high safety, high energy density, low cost, and no pollution. However, the sluggish redox kinetics of polyiodide conversion and the severe shuttle effect result in the degradation of active substances and corrosion of zinc anodes. Therefore, designing and developing a high-performance host material with high conductivity, high adsorption, and satisfactory catalytic activity can effectively confine polyiodides and facilitate the bidirectional redox kinetics, which is an urgent direction that needs to be developed. Hence, honeycomb shaped Zn dual atom sites embedded in nitrogen doped carbon nanosheets were designed to enhance the conversion of I_2. The well-designed Zn dual atom site structure can promote orbital hybridization between Zn and I atoms through orbital coupling between Zn sites and the substrate, thereby accelerating the bidirectional redox process of iodine and exhibiting satisfactory electrochemical performance.

Introduction

With the increasing depletion of traditional fossil fuels and serious environmental pollution, lithium-ion batteries have become some of the most promising energy storage devices. However, their serious safety issues due to the problems of lithium dendrite growth, limited lithium resources, and relatively high costs have hindered their further large scale development.[1–4] Rechargeable aqueous metal-ion batteries are promising energy storage devices due to their advantages of high safety, no pollution, long lifespan, and low processing costs.[5–7] Among the various aqueous batteries, aqueous zinc–iodine ($Zn–I_2$) batteries are increasingly becoming a research hotspot, which is ascribed to their high theoretical capacity (211 mA h g^{-1}) and energy density, excellent safety, satisfying

[a] *State Key Laboratory of Advanced Technology for Materials Synthesis and Processing, International School of Materials Science and Engineering, Wuhan University of Technology, Wuhan 430070, P. R. China. E-mail: xuxu@whut.edu.cn, mlq518@whut.edu.cn*

[b] *Zhongyu Feima New Material Technology Innovation Center (Zhengzhou) Co., Ltd, High Technology Industrial Development Zone, Zhengzhou 450001, P. R. China*

[c] *School of Materials Science and Engineering, Beihang University, 100191, Beijing, China*

[d] *State Key Laboratory of Medicinal Chemical Biology, Key Laboratory of Functional Polymer Materials, College of Chemistry, Nankai University, Tianjin 300071, China*

† Electronic supplementary information (ESI) available. See DOI: https://doi.org/10.1039/d4ee05767h

‡ C. X. D. and Y. K. Y. contributed equally to this work.

rate and cycle performance, abundant reserves and low cost (Zn storage: 75 ppm, iodine storage: 55 μg L^{-1}).[8–11] Nevertheless, to achieve state-of-the-art Zn–I_2 batteries, some key scientific challenges such as sluggish kinetics and the shuttle effect of polyiodides remain to be addressed. Specifically, during the redox reaction of I_2/I^-, some highly soluble intermediary products such as I_3^- and I_5^- migrate uncontrollably to the anode due to concentration gradients and react with the Zn anode, resulting in corrosion of the Zn anode, low coulombic efficiency and loss of active substances.[12–16] Moreover, the low conductivity of iodine and high energy barrier of the conversion between I_3^- and I^- lead to sluggish redox reactions and exhibit unsatisfactory rate performance.[17–21] To address these challenges, there are some methods for developing high-performance cathodes, modifying separators, introducing electrolyte additives to reduce the shuttle of polyiodides, building a protective layer of the Zn anode to prevent the side reaction of the Zn anode and so on to improve the performance of Zn–I_2 batteries.[22–26] Among them, the restriction of polyiodides into the host materials is regarded as a prominent strategy because it directly mitigates polyiodide shuttling as well as low iodine conductance. Porous carbon materials such as activated carbon and carbon nanotubes were taken as effective hosts to confine and adsorb polyiodides. However, the adsorption ability is so weak and lacks enough catalytic sites to accelerate the conversion of polyiodides that it makes it difficult to improve the performance of Zn–I_2 batteries.[27–30] Subsequently, some polar materials such as metal nitrides, metal oxides and metal organic frameworks were introduced to improve the electrocatalytic performance. Although the rate performance has been improved to some extent, the use of a large number of catalysts has resulted in a low proportion of active substances (<60%), which seriously affects the gravimetric and volumetric energy density of Zn–I_2 batteries.[31–34] Therefore, designing and developing cathode materials with high conductivity, high adsorption, satisfactory catalytic activity and efficiency for iodine and polyiodides is one of the hot research directions.[35–37]

Single-atom catalysts (SACs) have received increasing attention in Zn–I_2 batteries due to their highly efficient catalytic performance at low loads, and maximum atomic utilization, which has potential for achieving high energy density Zn–I_2 batteries.[38,39] Anchoring SACs into a porous carbon framework is beneficial for meeting the requirements of the cathode mentioned above, achieving effective adsorption and catalytic conversion of polyiodides.[19] Jin *et al.* developed a Ni single atom dispersed in porous carbon skeletons (NiSAs-HPC) to accelerate the redox reaction of polyiodides.[40] In another example, Zhang *et al.* prepared a single Fe atom embedded into the doughnut-like porous carbon (B–Fe–NC) to invoke the redox conversion of iodine.[29] These strategies indeed improve the electrochemical performance of Zn–I_2 batteries to some extent, but single atom catalysts stand out in one aspect of oxidation or reduction reactions in general. For the two reverse oxidation and reduction processes of I_2, the imbalance of adsorption and desorption abilities of single atoms limits the conversion of reactants and intermediates, thereby affecting the reversible deposition and stripping of I_2, which results in the challenge of sluggish conversion of polyiodides not being fundamentally solved.[41,42] To this end, benefiting from a richer electronic structure and activity, dual-atom catalysts (DACs) which link SACs and nanoparticle/cluster catalysts to optimize the adsorption/desorption ability by orbital coupling and hybridization are expected to become one of the solutions to address the aforementioned challenges.[43] More impressively, the synergistic effect of DACs not only overcomes the limitation of SACs *via* improving the formation and desorption of intermediates, but also activates iodine species due to more abundant metal active sites, thereby facilitating fast redox kinetics of polyiodides on the adjacent active sites.[44] However, the difficulty of synthesizing DACs and the complexity of catalytic mechanisms during the reaction process make it a blank space in Zn–I_2 batteries. In addition, the intrinsic connection between the orbital coupling of DACs structure and the kinetics of the polyiodide reaction remains unclear. Therefore, it is urgent to develop high-performance DACs to construct state-of-the-art Zn–I_2 batteries, and to thoroughly reveal the intrinsic mechanism of DACs promoting redox kinetics of polyiodides, which has never been reported.

In this study, we have designed honeycomb shaped Zn DACs embedded in nitrogen doped carbon nanosheets as the iodine host with a novel co-pyrolysis method to investigate the electrocatalytic performance of dual atoms for Zn–I_2 batteries for the first time. The Zn dual atom sites were clearly verified by microscopic and spectroscopic methods. In addition, electrochemical tests and theoretical calculations demonstrate that Zn dual atom sites not only enhance the adsorption of I_2, but also accelerate the redox kinetics of polyiodides. As a result, the batteries with the I_2@Zn_2NC cathode exhibit satisfactory capacity and cycle stability. The batteries show a high capacity of 205 mA h g^{-1} at 0.5C and achieve a capacity retention rate of 98% after 100 cycles. More impressively, the batteries reached the longest cycle life of 100 000 cycles at a high current density of 50C with a good capacity retention of 79% after 100 000 cycles. Furthermore, this work investigates the low-temperature performance of the I_2@Zn_2NC cathode, and achieves 7000 cycles at a high current density of 10C even at −20 °C.

Results and discussion

The preparation method of Zn_2NC through co-pyrolysis of a carbon-based Zn–citric acid complex and dicyandiamide and the working mechanism of the I_2@Zn_2NC cathode are unveiled in Fig. 1a and Fig. S1 (ESI†). In particular, the pyrolysis of sodium citrate tribasic dihydrate provides a porous honeycomb shaped carbon substrate, which is beneficial for loading and adsorption of I_2. The zinc acetate dihydrate was used as a zinc source to prepare single Zn atoms. Subsequently, the citric acid monohydrate was used as a chelating agent to form Zn–citric acid complexes adsorbing onto the carbon matrix and was pyrolyzed with dicyandiamide which was used as a nitrogen source, ultimately to obtain the Zn_2NC dual metal atom catalyst.

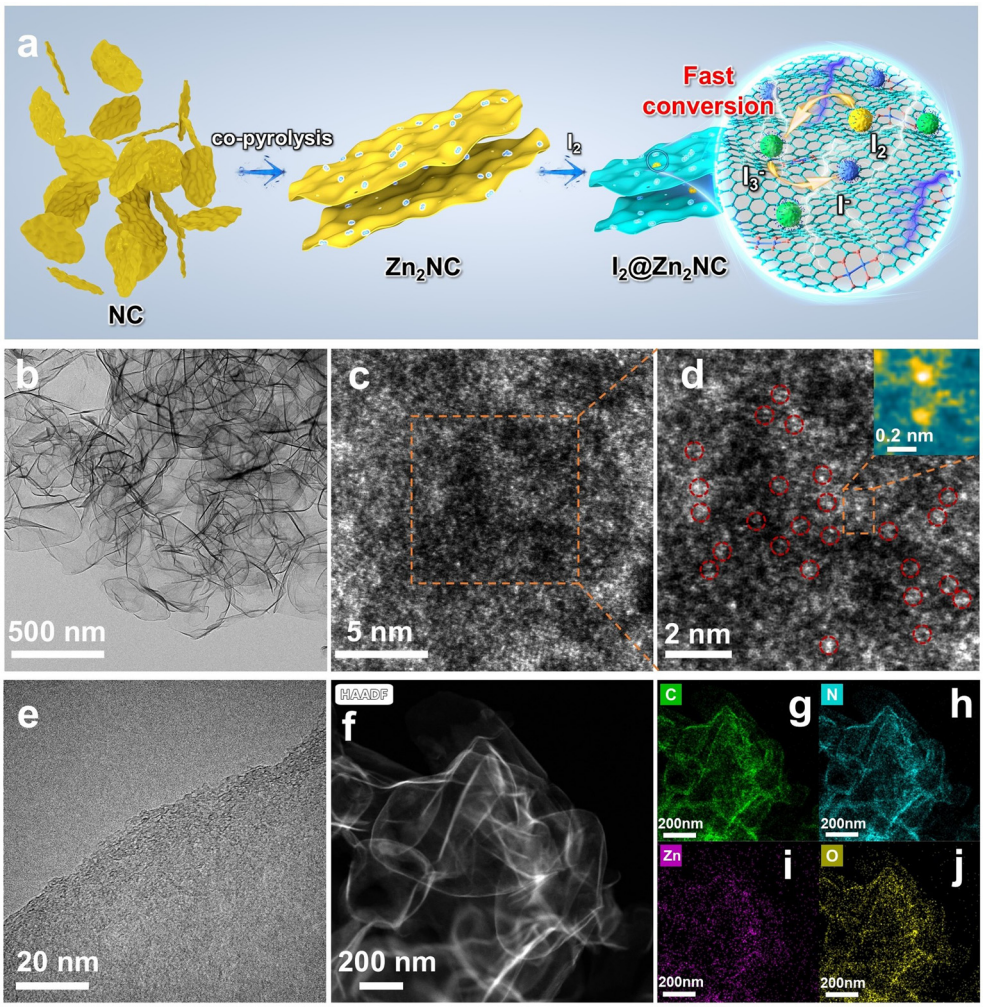

Fig. 1 (a) Schematic illustration of the preparation procedure and working mechanism of I_2@Zn_2NC. (b) The TEM images of Zn_2NC. (c) Atomic-resolution HAADF-STEM image of Zn_2NC. (d) Enlarged intensity image of Zn_2NC and the Zn dual atoms in the observed diatomic pair. (e) HRTEM image. (f)–(j) STEM image and corresponding elemental mapping images of Zn_2NC.

Firstly, scanning electron microscopy (SEM) and transmission electron microscopy (TEM) were conducted to characterize the morphology of Zn_2NC and control samples. As shown in Fig. S2 (ESI†), Zn_2NC exhibits a honeycomb shaped morphology formed by interlacing nanosheets, which is similar to ZnNC (Fig. S3, ESI†) and NC (Fig. S4, ESI†), manifesting dual atom sites have little effect on the whole morphology. More importantly, the synergetic effect of the honeycomb shaped carbon substrate and dual atom active sites is conducive to iodine adsorption and catalysis benefitted from the morphology design. In addition, Fig. 1b also exhibits the interlacing nanosheets morphology, which is consistent with SEM results. Furthermore, to further characterize the dual atom sites, aberration-corrected high-angle annular dark-field scanning TEM (AC-HAADF-STEM) was conducted to intuitively observe the distribution of dual single atoms. A large number of couple bright spots can be observed in Fig. 1c, representing the Zn dual atom sites on the Zn_2NC catalyst. The locally enlarged image further illustrates the existence of diatomic sites in Fig. 1d. The AC-HAADF-STEM images of ZnNC show more single bright dots than that of Zn_2NC, manifesting single Zn sites dominate in ZnNC (Fig. S5, ESI†). The zinc content in the Zn_2NC and ZnNC is 1.71 wt% and 1.47 wt% according to the inductively coupled plasma optical emission spectrometry (ICP-OES) analysis. XRD patterns were further conducted to analyze the crystallization structure of Zn_2NC in Fig. S6 (ESI†). Two broad diffraction peaks around 25° and 52° correspond to the (002) and (101) crystal planes, which conform to the diffraction peak of graphene carbon.[25]

In addition, the XRD pattern of Zn_2NC is similar to those of ZnNC and NC, demonstrating no formation of Zn clusters or nanoparticles. The HRTEM image further proves the poor crystallization of Zn_2NC, which is consistent with XRD broad diffraction peaks (Fig. 1e). As shown in Fig. 1f and Fig. S7 (ESI†), the HADDF-STEM and element mapping images prove the uniform distribution of Zn, N and C elements without obvious clusters of Zn_2NC and ZnNC. Moreover, Raman spectra were conducted to characterize the lattice defect of different examples. There are two peaks at $\sim$1339 cm^{-1} and $\sim$1563 cm^{-1}, which represent the D band and G band of sp^2-hybridized carbon atoms. The I_D/I_G (I_D and I_G represent the intensity of D

and G bands) of Zn_2NC (1.15) is larger than that of ZnNC (1.08) and NC (1.05), which reveals that Zn_2NC possesses the greatest disorder compared with the other examples (Fig. S8, ESI†). Besides, the Brunauer–Emmett–Teller (BET) test reveals a typical type IV isotherm with a large specific surface and a high pore volume, which is beneficial for I_2 adsorption and confinement (Fig. S9, ESI†). Thanks to this, the Zn_2NC is able to achieve up to 78% high I_2 loading, which is demonstrated by thermogravimetric analysis (Fig. S10, ESI†). Furthermore, the SEM images and EDS mapping of I_2@Zn_2NC after I_2 loading exhibit similar morphology with Zn_2NC and no blocky iodine was observed, proving the uniform dispersion of iodine on the interleaved nanosheets (Fig. S11 and S12, ESI†). Because electron irradiation and a high vacuum environment will cause iodine sublimation, the weight ratio Zn, N, I and C is 1.27 wt%, 0.88 wt%, 2.78 wt% and 95.07 wt% (Fig. S13 and Table S1, ESI†).

X-ray photoelectron spectroscopy (XPS) analysis was conducted to investigate the existence and chemical environment of Zn, N and C elements. The high-resolution XPS spectrum at the C region shows three peaks at 287.8 eV, 285.8 eV and 284.8 eV, which represent the C–O–C, C–N and C═C bonds, respectively, demonstrating the successful introduction of N heteroatoms (Fig. 2a). As shown in Fig. 2b, the N 1s spectrum displays the pyrrolic N at 400.6 eV, graphitic N at 403.6 eV and pyridinic N at 398.7 eV, respectively. The incorporation of N species is instrumental in constructing a positive surface to improve the chemical adsorption of iodine species by polarization interaction. Moreover, the Zn–N peak is also observed at 399.8 eV in the N 1s spectrum, which proves the direct interaction between Zn and N atoms. In the Zn 2p spectrum, there are four peaks at 1045.2 eV, 1022.1 eV, 1047.5 eV, and 1023.1 eV, which are ascribed to $2p_{1/2}$, $2p_{3/2}$ splitting of Zn and $2p_{1/2}$, $2p_{3/2}$ splitting of Zn–N[43] (Fig. 2c). These results further demonstrate the effective introduction of N heteroatoms, Zn single atoms and the formation of Zn–N coordination environment. Additionally, to further characterize the coordination information and local structure of Zn dual atom sites at the atomic level, synchrotron-radiation-based X-ray absorption near-edge structure (XANES) spectra and Fourier-transformed extended X-ray absorption fine structure (FT-EXAFS) characterization were conducted. The Zn K-edge XANES spectra analyzed the near-edge structure of Zn_2NC and control samples in which

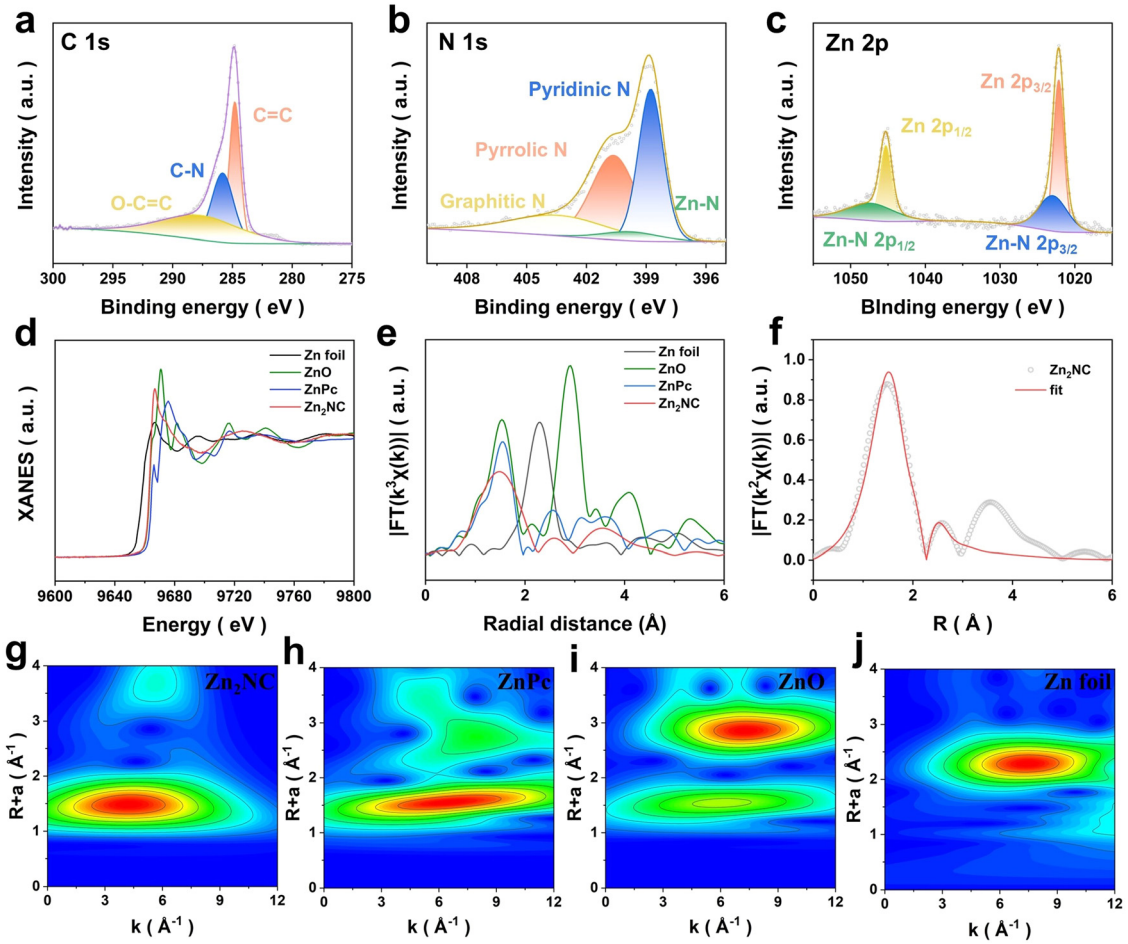

Fig. 2 (a) C 1s, (b) N 1s, and (c) Zn 2p XPS spectra of Zn_2NC. (d) Zn K-edge X-ray absorption near edge structure (XANES) spectra of Zn_2NC, ZnO, ZnPc and Zn foil. (e) Corresponding FT results at the Zn K-edge. (f) FT-EXAFS fitting curves in the *R* space fitting curves of Zn_2NC. (g)–(j) Zn K-edge WT-EXAFS contour plots of different samples.

the line position of Zn_2NC is located between Zn foil and ZnO, manifesting that the valence state of Zn in Zn_2NC is between 0 and +2 (Fig. 2d). To further investigate the coordination information, the FT-EXAFS spectra exhibit two dominant peaks at 1.5 Å and 2.5 Å, which are ascribed to the Zn–N and Zn–Zn scattering paths in *R*-space, demonstrating that the coordination of Zn is mainly Zn–N coordination, and there are also Zn–Zn dual-atom sites present (Fig. 2e). Moreover, as shown in Fig. 2f, the fitting curves of the EXAFS spectra display two dominant peaks at 1.5 Å and 2.48 Å, which are attributed to the Zn–N and Zn–Zn coordination. Based on these results, the most likely Zn_2N_6 coordination structure was obtained (Fig. S14, S15 and Table S2, ESI†). The wavelet transform (WT) analysis was further conducted to provide clear information on backscattering atoms in *R* and *k* space. The contour plot of Zn_2NC displays a WT maximum at about 4.5 Å, which is close to that of ZnPc, demonstrating that the Zn atom mainly coordinates with light atoms but differs from the Zn–O bond in ZnO (Fig. 2g–j). These outcomes prove Zn–Zn dual atom sites and Zn–N coordination in Zn_2NC catalysts. To further prove the structure difference between the ZnNC and Zn_2NC catalysts, we have obtained the XANES spectra and FT-EXAFS data of ZnNC as a comparison. The Zn K-edge XANES spectra analyzed the near-edge structure of ZnNC and control samples in which the line position of ZnNC is also located between Zn foil and ZnO, manifesting that the valence state of Zn in ZnNC is between 0 and +2. Moreover, the fitting curves of the FT-EXAFS spectra exhibit two peaks at 1.53 Å and 2.70 Å and the fitting results demonstrate the Zn–N_4 coordination structure (Table S2, ESI†). Comparison with Zn_2NC reveals a significant deviation in the position of the Zn–Zn bond thus leading to a change in the coordination structure, which in turn demonstrates the successful synthesis of Zn_2NC and ZnNC catalysts (Fig. S16, ESI†).

To further investigate the catalytic performance of Zn dual atom sites for redox reaction of I_2, symmetrical batteries were assembled with I_3^- electrolyte for cyclic voltammetry (CV) measurements. Two different peaks can be observed during the redox conversion of polyiodides for Zn_2NC and ZnNC, manifesting that Zn single atoms are able to facilitate the redox reaction (Fig. 3a). And the response current density of Zn_2NC is larger than that of ZnNC, which proves that Zn dual atom sites could further improve the redox kinetic of polyiodides. In

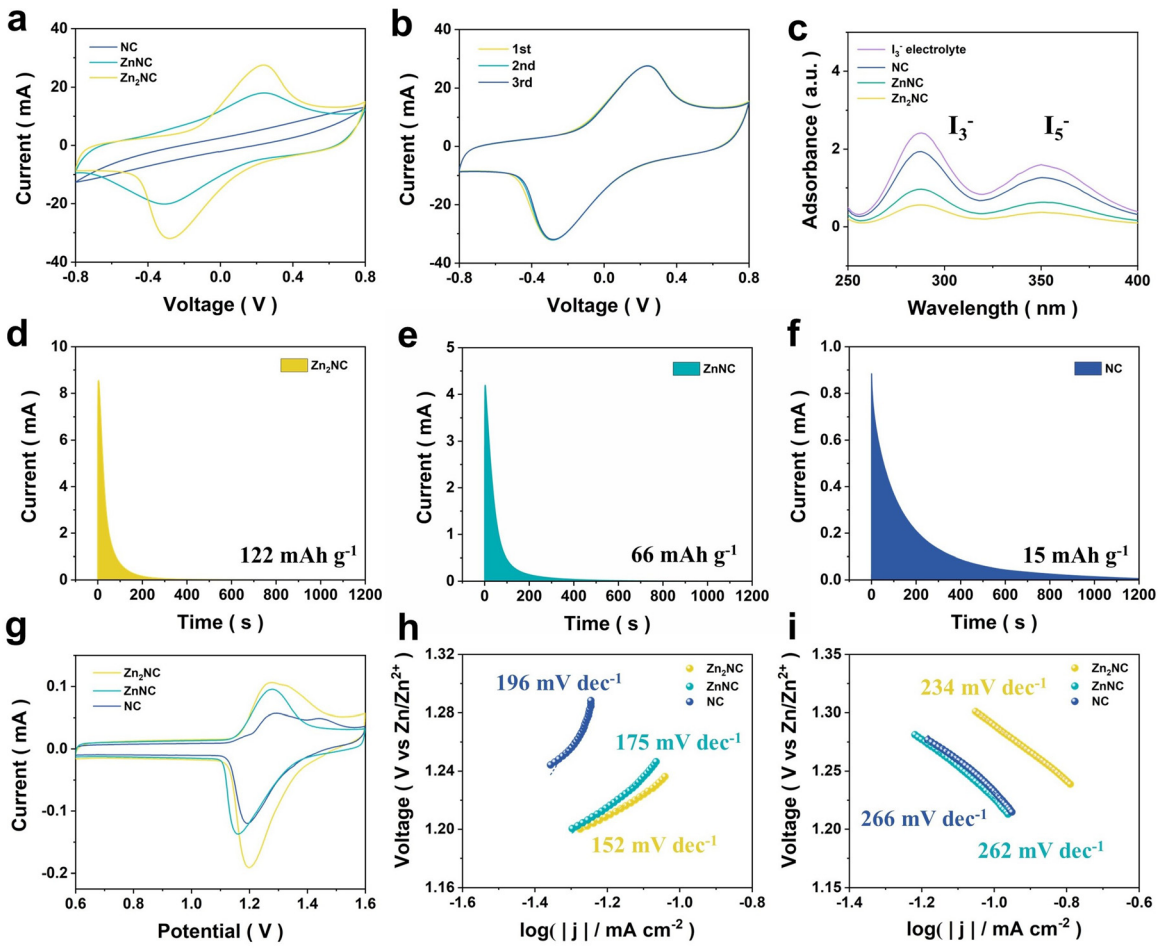

Fig. 3 (a) and (b) Cyclic voltammetry (CV) curves and the first three cycles of CV curves for the symmetric batteries at a scan of 50 mV s^{-1}. (c) UV-vis absorption spectra of the adsorption test. (d)–(f) Potentiostatic deposition tests with (d) Zn_2NC, (e) ZnNC, and (f) NC. (g)–(i) CV curves at 0.1 mV s^{-1} and derived Tafel plots of different composites.

comparison, there are no obvious redox peaks in the CV curve of NC, which is ascribed to the lack of catalytic active sites. Moreover, the CV curves of the initial three cycles for Zn_2NC show good coincidence, manifesting satisfactory reversibility during the redox process of polyiodides (Fig. 3b). The adsorption ability for polyiodides also determines the performance of Zn–I_2 batteries, so we conducted visual adsorption tests and UV-vis spectroscopy on different substrates with 0.02 mol L^{-1} I_3^- solution. As shown in Fig. S17 (ESI†), the solution with the Zn_2NC catalyst turned colorless and transparent after standing for 6 h, while the other three control samples still maintained the color of the I_3^- solution, which indicates Zn_2NC has more advantages in adsorbing polyiodides compared to other controls. In addition, the UV-vis spectroscopy of the solution after standing shows two peaks at about ~290 nm and ~350 nm which are ascribed to I_3^- species, and the peak intensity of Zn_2NC is significantly lower than the other three systems, proving Zn_2NC almost absorbed I_3^- species in the solution completely[21] (Fig. 3c). To further study the adsorption capacity of different samples, we tested the intensity of standard UV peaks at different concentrations to determine the concentration of the solution after the adsorption of I_3^- by the catalysts. In the actual test, the solution to be measured was diluted 20 times in order to avoid the intensity exceeding the range. Based on the results of the fitting and the intensities of the absorption peaks, the I_3^- absorption by Zn_2NC, ZnNC and NC can be calculated as 8.9 mg, 6.7 mg and 2.4 mg (Fig. S18, ESI†). These results manifest the stronger adsorption ability of Zn_2NC may be attributed to the Zn dual atom sites and more Zn active sites. The XPS spectra of iodine after being adsorbed onto the Zn_2NC can be fitted with three pairs of coupling peaks at 619.2/630.7 eV, 620.0/631.5 eV and 621.0/632.9 eV, which is ascribed to I_3^-, I_2 and I_5^- species, respectively, demonstrating strong interaction between iodine species with Zn_2NC (Fig. S19, ESI†). More impressively, potentiostatic nucleation experiment was conducted to analyze the ability of different hosts for facilitating I_2 deposition from I_3^- species. The I_2 nucleation test is similar to the Li_2S nucleation test, which means that the response current density and peak area reflect the activity of the catalyst and interface reaction kinetics. As shown in Fig. 3d–f, the Zn_2NC substrate shows a high response current as high as 8.5 mA, which is significantly higher than that of ZnNC (4.2 mA) and NC (0.9 mA). In addition, the calculated deposition capacity of Zn_2NC is 122 mA h g^{-1}, while the ZnNC and NC electrode only exhibits 66 mA h g^{-1} and 15 mA h g^{-1}, respectively. Moreover, the decomposition of ZnI_2 also shows the highest capacity with Zn_2NC (182 mA h g^{-1}) than with ZnNC (111 mA h g^{-1}) and NC (43 mA h g^{-1}) (Fig. S20, ESI†). These results indicate that Zn dual atom sites in Zn_2NC are conducive to accelerating the bidirectional redox reaction kinetics of I_2.

To further investigate the effect of Zn dual atom sites on the electrochemical performance of Zn–I_2 batteries, the full Zn–I_2 batteries were assembled with I_2@Zn_2NC cathodes and other control cathodes (I_2@ZnNC and I_2@NC). As shown in Fig. 3g, the CV curve of Zn_2NC exhibits one pair of redox peaks at 1.20 V and 1.27 V, which is attributed to the oxidation and reduction reaction of I_2/I^-. In addition, the I_2@Zn_2NC cathode shows a lower potential polarization and higher current response than the other two systems, indicating satisfactory reversibility of the I_2@ZnNC cathode. In addition, the Zn_2NC exhibits the biggest area compared with the other samples, manifesting that the redox reactions transfer more charge (Fig. S21, ESI†). Moreover, the Tafel slope calculated from the CV curves further proves the bidirectional improvement for the redox reaction of I_2/I^- with Zn dual atom sites (Fig. 3h and i). The Zn_2NC shows a low Tafel slope with 152 mV dec^{-1} calculated from the oxidation peak, which is smaller than that of ZnNC (175 mV dec^{-1}) and NC (196 mV dec^{-1}). For the reduction process, the Tafel slope of Zn_2NC is 234 mV dec^{-1}, which is also smaller than that of ZnNC (262 mV dec^{-1}) and NC (266 mV dec^{-1}). In addition, we have conducted EIS testing to characterize interface impedance. The I_2@Zn_2NC cathode shows a lower charge transfer resistance than the other electrodes, manifesting faster charge transfer kinetics (Fig. S22, ESI†). These outcomes demonstrate that the Zn dual atom sites are able to optimize the adsorption/desorption ability for polyiodides and facilitate the reaction kinetics for the redox conversion of I_2/I^-.[18] The CV curves of Zn_2NC at the initial three cycles were studied to analyze the reaction reversibility (Fig. S23, ESI†). The three curves all display two obvious redox peaks and good coincidence, manifesting satisfactory reversibility and stability. The multiscan CV curves from 0.1–0.5 mV s^{-1} were conducted to investigate the effect of scan rates on the redox reaction (Fig. S24, ESI†). The response current increases and redox peaks shift slightly with the increasing of scan rates. And curves of Zn_2NC still exhibit obvious redox peaks even at high scan rates, indicating the stable redox reaction of polyiodides with the Zn_2NC host. Moreover, the self-discharge tests were conducted under a high I_2 content of 2.5 mg cm^{-2}. The batteries with I_2@Zn_2NC show low self-discharge and achieve high coulombic efficiency of 99.5%, which is higher than that of I_2@ZnNC and I_2@NC (Fig. S25, ESI†).

The effect of Zn dual atom sites on the cycle performance of Zn–I_2 full cells was first investigated at a low current density of 0.5C (Fig. 4a). The batteries with I_2@Zn_2NC cathodes exhibit a high initial specific capacity of 208 mA h g^{-1}, which is significantly higher than that of ZnNC (186 mA h g^{-1}) and NC (125 mA h g^{-1}), manifesting the Zn dual atoms activate more I_2 species and catalyze the conversion of polyiodides, thereby providing more capacities. Additionally, the batteries with I_2@Zn_2NC cathodes show good cycle stability, with a capacity retention rate of 98% after 100 cycles, which is ascribed to the enhanced redox reaction and smaller shuttle effect with adsorption and catalysis of Zn dual atom sites. The voltage polarization of the I_2@Zn_2NC cathode is 50 mV, which is lower than that of I_2@ZnNC (70 mV) and I_2@NC (90 mV), indicating fast redox kinetics of the I_2@Zn_2NC electrodes (Fig. 4b). Furthermore, the rate performance of Zn–I_2 batteries with different cathodes was analyzed at a current density from 0.5C to 50C. The batteries with I_2@Zn_2NC cathodes exhibit a capacity of 212 mA h g^{-1}, 195 mA h g^{-1}, 180 mA h g^{-1}, 162 mA h g^{-1}, 139 mA h g^{-1}, 120 mA h g^{-1} and 105 mA h g^{-1} at 0.5C, 1C, 2C, 5C, 10C, 20C and 50C, respectively (Fig. 4c). In comparison, the I_2@ZnNC and I_2@NC cathodes only provide

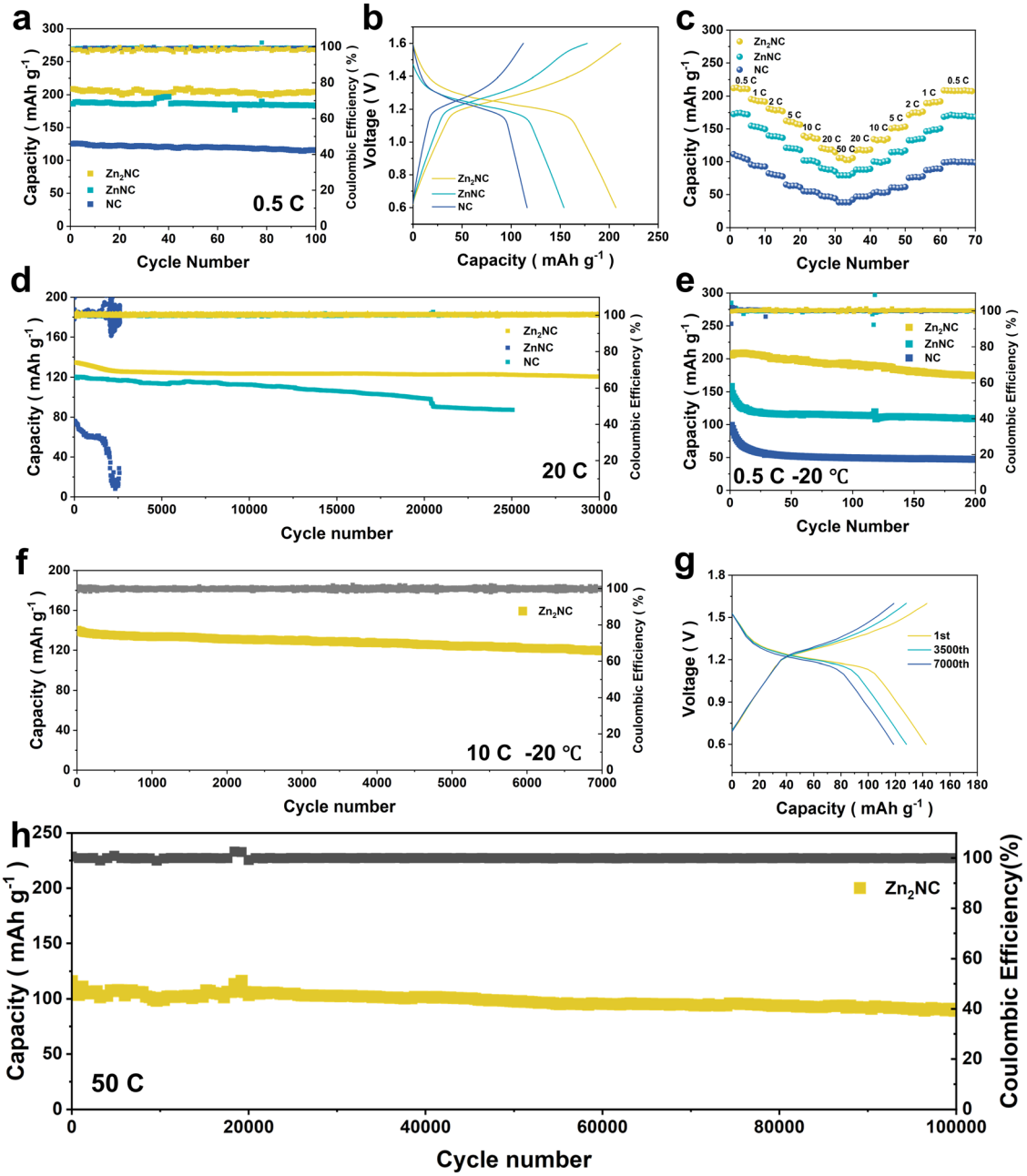

Fig. 4 (a) Cycling performances at 0.5C. (b) Galvanostatic charge–discharge curves at a current density of 0.5C. (c) Rate performances of I_2@Zn_2NC, I_2@ZnNC, and I_2@NC cathodes. (d) Long cycling performances at 20C. (e) Cycling performances at 0.5C at −20 °C. (f) Long cyclic performances with different cathodes at 10C at −20 °C. (g) Galvanostatic charge–discharge curves at a current density of 10C at −20 °C. (h) Long cycling performance of the I_2@Zn_2NC electrode at 50C.

capacities of 79 mA h g^{-1} and 39 mA h g^{-1} at 50C, indicating Zn dual atom sites could enhance the redox kinetics by regulating the adsorption/desorption relationship of reactants and intermediates. The voltage plateau at different rates of different cathodes is shown in Fig. S26 (ESI†). The I_2@Zn_2NC cathodes display stable charge and discharge plateau even at a high rate of 50C, while the plateau of I_2@ZnNC and I_2@NC are inconspicuous at high rates, thereby demonstrating remarkable rate performance with the Zn_2NC host. To further study the cycle performance of the I_2@Zn_2NC cathode, long cycle performances at high current densities were conducted. As shown in Fig. S27 (ESI†), the I_2@Zn_2NC cathode exhibits a high initial capacity of 146 mA h g^{-1} and retains a capacity of 141 mA h g^{-1} after 5000 cycles at 10C with a capacity retention of 96.6%. At a higher current density of 20C, the batteries with I_2@Zn_2NC cathodes display a high initial capacity of 134 mA h g^{-1} and maintain a capacity retention of 90.9% after 30 000 cycles. The I_2@ZnNC cathode only provides an initial capacity of 119 mA h g^{-1} with a low capacity retention of 73%. The sudden decrease in capacity around 20 000 cycles is

attributed to the difficulty of balancing adsorption–desorption relationships with Zn single atoms, which reduces catalytic ability and ultimately leads to a decrease in capacity. The batteries with I_2@NC cathodes show a low capacity of 76 mA h g^{-1} and the batteries have almost no remaining capacity after 2500 cycles, which is attributed to the lack of active sites to catalyze the conversion of polyiodides (Fig. 4d). Even the current rate was increased to 50C, the I_2@Zn_2NC still provides a high capacity of 114.6 mA h g^{-1} and exhibits an ultralong and ultrastable cycle performance with an ultralow capacity fading rate of 0.0002% per cycle after 100 000 cycles, which is the longest cycle at present for aqueous Zn–I_2 batteries (Fig. 4h). Additionally, the voltage plateau of the battery still shows stable redox reaction at the 1st, 50 000th and 100 000th cycles (Fig. S28, ESI†), indicating the Zn dual atom sites could catalyze the conversion of polyiodides efficiently and persistently even at high rates. To further investigate the catalytic ability of the Zn dual atom sites in the Zn_2NC catalyst for polyiodides, an electrochemical cycle performance test was conducted under extremely low-temperature conditions. To eliminate the influence of the electrolyte on battery performance under low temperature conditions, 3 M $Zn(ClO_4)_2$ was used as the electrolyte to test the low-temperature cycling performance. Firstly, we tested the CV curves with different cathodes at −20 °C (Fig. S29, ESI†). Similar to room temperature, the CV curves show one pair of redox peaks, ascribed to the oxidation and reduction of I_2/I^-. The Zn_2NC@I_2 cathode still exhibits lower voltage polarization, higher current response and closed area, indicating the outstanding performance of Zn_2NC at low temperature. In addition, the rate performance with different samples was conducted to characterize the redox kinetics of batteries at low temperature (Fig. S30,ESI†). The cells with the I_2@Zn_2NC cathode show satisfactory rate performance compared with the other two samples, especially at high current densities. The cell with I_2@Zn_2NC still exhibits a capacity of 63 mA h g^{-1} at 50C, while the capacity of the other samples is almost negligible. Moreover, the galvanostatic charge–discharge profiles of the batteries with I_2@Zn_2NC cathodes display two charge–discharge plateaus, which are ascribed to the oxidization and reduction processes and are consistent with the results of the CV curves (Fig. S31, ESI†). Even at a high rate of 50C, the batteries with I_2@Zn_2NC cathodes still exhibit two redox platforms, while the plateaus of the other two systems disappear. Low-temperature *in situ* spectroscopy was also conducted with refrigeration equipment and a Raman spectrometer (Fig. S32, ESI†). The Raman peak intensity also shows a similar trend of change, indicating a similar mechanism of the polyiodide oxidation–reduction process. Despite the slow kinetics and severe shuttle effect at low temperatures, the I_2@Zn_2NC cathode can still effectively adsorb and catalyze the conversion of polyiodides, exhibiting lower peaks of I_3^- and I_5^- (Fig. S33, ESI†). These results suggest that the Zn_2NC catalyst has superior catalytic properties and thus is able to accelerate polyiodide conversion. As shown in Fig. 4e, the batteries with the I_2@Zn_2NC cathode still exhibit a high specific capacity of 205 mA h g^{-1}, and retain a capacity of 174 mA h g^{-1}, thereby achieving a high capacity retention of 84.9% after 200 cycles at 0.5C. As a comparison, the I_2@ZnNC and I_2@NC batteries only provide a low initial capacity of 158 mA h g^{-1} and 99 mA h g^{-1}, indicating that Zn dual atom site catalysts still possess high catalytic activity even at low temperature.

Moreover, even at a high current density of 10C, the batteries assembled with I_2@Zn_2NC cathodes still provide a high capacity of 140 mA h g^{-1}, and show a low capacity fading rate of 0.002% per cycle after 7000 cycles, which proves that Zn dual atom sites facilitate redox kinetics of polyiodides even at a low temperature of −20 °C (Fig. 4f). Additionally, the voltage plateau of the 1st, 3500th, and 7000th cycles also display good oxidation and reduction reactions, demonstrating the satisfactory catalytic performance of Zn_2NC for polyiodides redox reactions (Fig. 4g). These results further certificate that the Zn dual atom sites still possess high catalytic activity for polyiodides conversion and restrict the shuttle effect even at low temperature, thereby improving the cycle performance at −20 °C. In the case of high iodine loading, the shuttle effect of polyiodides will be more severe, so it is necessary to test the electrochemical performance under high iodine loading to demonstrate its application prospects. The high iodine loading performance was tested with 5.1 mg cm^{-2} and 19.1 mg cm^{-2} at 1C, at which initial areal capacities of 0.82 mA h cm^{-2} and 2.86 mA h cm^{-2}, and capacity retention rates of 97.7%, and 84.3% after 150 cycles were achieved (Fig. S34, ESI†). In order to further verify the practical application potential of Zn_2NC, a pouch cell was assembled at 0.5C. The pouch cell exhibits a high initial capacity of 170 mA h g^{-1} and maintains its capacity of 125 mA h g^{-1} after 40 cycles, demonstrating the well-running of the Zn–I_2 pouch cell (Fig. S35, ESI†). In addition, we utilized SEM images to characterize the morphology of Zn_2NC after cycling. The Zn_2NC catalyst still maintains its porous honeycomb shaped structure after 20 cycles, which suggests the honeycomb shaped structure can effectively confine the polyiodides (Fig. S36, ESI†). Furthermore, to demonstrate the superiority of zinc dual single atom sites in Zn–I_2 batteries, this work is compared with other highly active cathode works (Table S3, ESI†). It can be found that the dual zinc atom catalyst has significant advantages in iodine loadings, low-temperature performance, cycle number, and cycle stability.

In order to further investigate the role of Zn dual single atoms in the redox process of polyiodides, *in situ* Raman testing was conducted at 0.5C. The *in situ* Raman spectroscopy of Zn–I_2 batteries with I_2@NC shows two peaks at ∼110 cm^{-1} and ∼170 cm^{-1}, which are corresponding to the I_3^- and I_5^- species, respectively (Fig. 5a). As the discharge proceeds, the Raman peak intensities of I_3^- and I_5^- decrease, indicating the reduction process of polyiodides (I_5^-–I_3^-–I^-). For the charging process, the Raman peak intensities of I_3^- and I_5^- increased until reaching their maximum at 1.6 V, indicating the continuous generation of I_3^- and I_5^- during the oxidation reaction. The second reaction process exhibited similar peak intensity changes, demonstrating the reversibility of polyiodides during battery operation (Fig. 5b and c). As a comparison, the peaks of I_3^- and I_5^- are not obvious during the electrochemical reaction

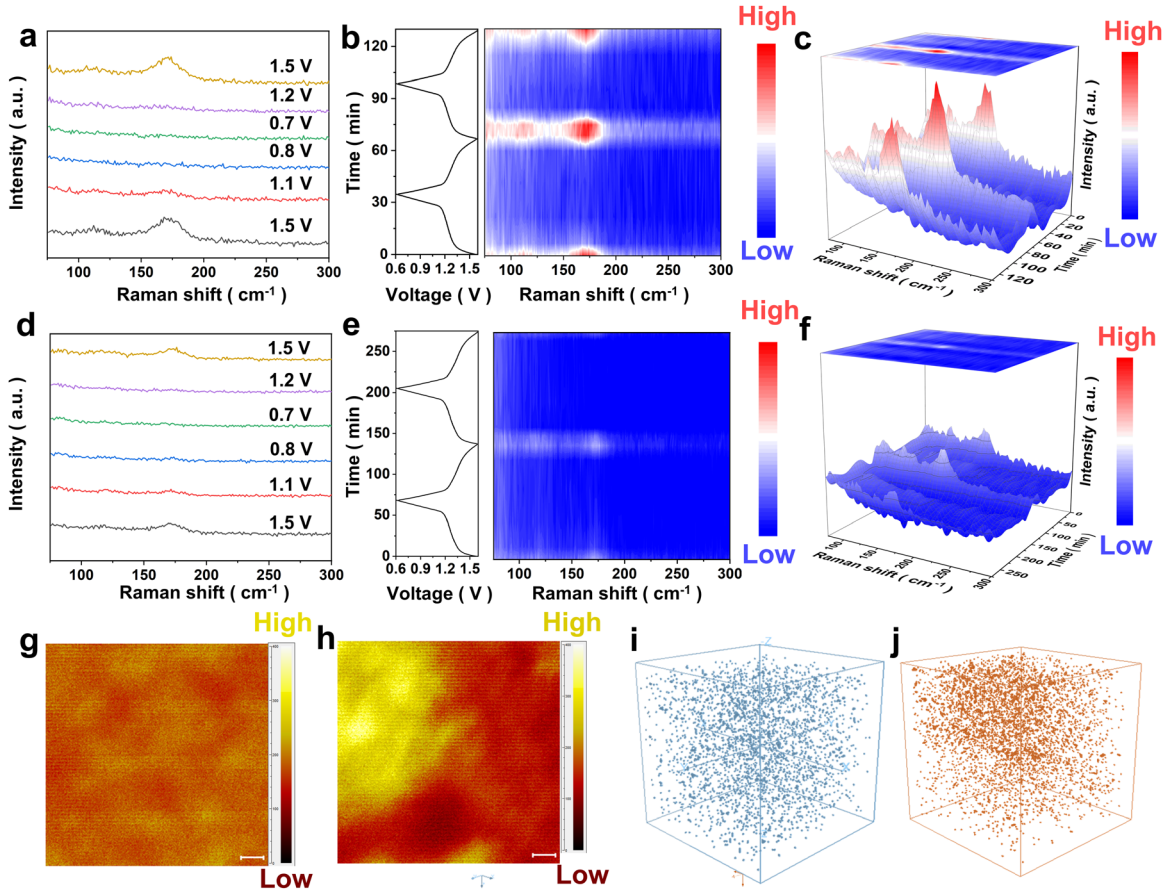

Fig. 5 (a) and (d) *In situ* Raman spectrum of I_2@NC and I_2@Zn_2NC. (b), (c), (e) and (f) The corresponding planar and 2D and 3D *in situ* time-resolved Raman spectra. (g) and (h) ToF-SIMS I^- element mappings on the top surface. (i) and (j) ToF-SIMS 3D rendering the I^- depth profile image.

processes in the Zn–I_2 batteries with I_2@Zn_2NC cathodes[36] (Fig. 5d–f). We also conducted the *in situ* Raman spectra of I_2@ZnNC, and it can be found that ZnNC is able to restrict the shuttling effect of polyiodides to a certain degree, but is slightly inferior to that of Zn_2NC, which further demonstrates the effective adsorption of polyiodides by dual single atoms (Fig. S37, ESI†). Considering the similar I_2 loading of the cathodes, these differences are attributed to the accelerated conversion of polyiodides by Zn dual atomic sites due to their excellent synergistic adsorptive and catalytic performance. Time-of-flight secondary ion mass spectrometry (ToF-SIMS) was used to further characterize the adsorptive and catalytic conversion effect of Zn dual atomic sites on polyiodides. The I_2@NC cathode displays higher intensities and blocky iodine distribution compared with that of I_2@Zn_2NC after 100 cycles at 5C, indicating insufficient I_2 species reaction due to the poor catalytic activity of the I_2@NC cathode (Fig. 5g, h and Fig. S38, ESI†). In addition, TOF-SIMS 3D images show that polyiodides in the I_2@NC cathode are mainly concentrated on the surface while polyiodides are uniformly distributed inside the catalysts with the I_2@Zn_2NC cathode, proving that Zn dual atomic sites can effectively adsorb polyiodides and suppress the shuttle effect (Fig. 5i and j). These outcomes demonstrate Zn dual atom sites are able to optimize the adsorption/desorption ability for polyiodides and accelerate the redox kinetics.

In order to gain a deeper understanding of the adsorption catalytic mechanism of Zn bimetallic atoms on iodine species, density functional theory (DFT) calculations were employed to investigate the atomic scale interaction mechanism. As shown in Fig. S39 (ESI†), optimized substrate configurations for Zn_2NC and the control samples were established to further calculate the interaction energy. The density of states (DOS) of Zn_2NC, ZnNC and NC were computed to explore the energy level distribution of different catalysts (Fig. S40, ESI†). The valence bands of Zn_2NC and the other two samples pass through the Fermi level, demonstrating electrochemical activity during the polyiodide conversion. Meanwhile, above the Fermi energy level, it is observed that Zn_2NC, ZnNC and NC exhibit the first distinct main peaks at 1.07 eV, 1.43 eV and 1.5 eV, indicating that the empty band energy level of Zn_2NC is closer to the Fermi level, which is more conducive to electron filling and adsorption of iodine molecules. To further prove the empty band energy level of Zn_2NC is closer to the Fermi level, the d-band-center of Zn_2NC and ZnNC were calculated. The d-band center of Zn_2NC (−3.78 eV) is larger than that of ZnNC (−5.73 eV), which indicates Zn_2NC is beneficial for the I_2 adsorption and activation. Moreover, the PDOS of Zn-d orbitals, N-p orbitals and C-p orbitals exhibit orbital coupling in the Zn_2NC substrate, which facilitates the upward shift of the

d-band center (Fig. S41, ESI†). In addition, the DOS of I_2 adsorption on different substrates reveals that the adsorption of I_2 by Zn_2NC is followed by the appearance of corresponding stronger characteristic peaks below the Fermi energy level as well as characteristic peaks closer to the Fermi energy, indicating that the electronic energy levels of Zn_2NC have larger electron rearrangement and orbital hybridization between the d-orbital electrons of the Zn dual atoms and the outermost electrons of I, proving that the interaction between Zn_2NC and I_2 is strengthened, which is more conducive to the adsorption of I_2 (Fig. 6d–f). As shown in Fig. S42 (ESI†), the PDOS of the I orbit further demonstrates that the strong electron transfer of I_2 exists after adsorbing on the Zn_2NC substrate. Furthermore, we constructed adsorption configurations of polyiodides on different substrates, demonstrating the Lewis acid–base interaction of Zn atoms on polyiodides (Fig. S43–S45, ESI†), and negative adsorption values indicate that the adsorption of polyiodides by catalysts is thermodynamically stable (Fig. 6g).

The adsorption energies of Zn_2NC are lower than that of the other two samples, manifesting stronger adsorptive abilities for polyiodides due to the synergetic effect of Zn dual atoms, which is consistent with visual test results. The simulated deformation charge density was further determined to reveal the charge transfer between different substrates and I_2. The I_2 exhibits a higher charge transfer on the Zn_2NC substrate (0.548 *e*) than the ZnNC (0.389 *e*) and NC (0.123 *e*), further manifesting the strong interaction between Zn_2NC and I_2 (Fig. 6a–c). The simulated deformation charge density of I_3^- on Zn_2NC, ZnNC, and NC indicates that the adsorption of I_3^- on NC is physisorption due to no electron cloud deformation and does not have subsequent reactivity. Whereas, the introduction of Zn atoms leads to the chemisorption of I_3^- on the substrate (Fig. S46, ESI†). Furthermore, the Gibbs free energy was conducted to study the spontaneity of polyiodide conversion (Fig. 6h). The Gibbs free energy of Zn_2NC (0.813 eV) is lower than that of ZnNC (0.871 eV) and NC (1.149 eV) for the rate-determining step of I_3^-/I^-, indicating Zn_2NC catalysts possess the most

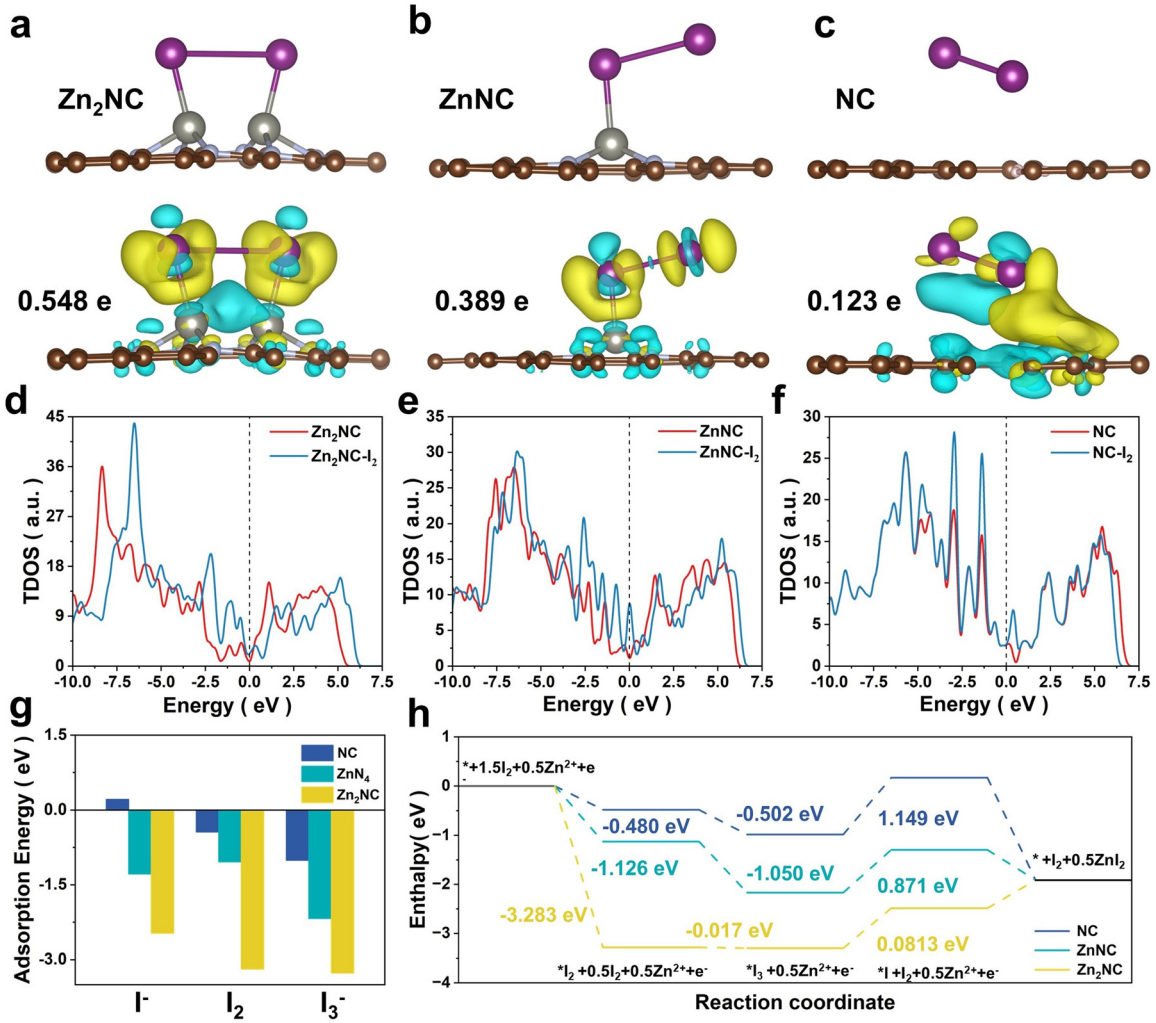

Fig. 6 (a)–(c) Simulated deformation charge density of I_2 on Zn_2NC, ZnNC, and NC. (d)–(f) TDOS of (d) Zn_2NC, (e) ZnNC and (f) NC orbitals before and after adsorption of I_2. (g) Calculated adsorption energy of various polyiodides adsorbed on different catalysts. (h) Gibbs free energy of the I_2 reduction process on Zn_2NC, ZnNC and NC.

satisfactory conversion kinetics for polyiodides ascribed to the synergetic adsorption-catalysis effect of Zn dual atoms. In addition, the reaction energy barrier of the Zn_2NC surface (0.94 eV) is lower than that of ZnNC (1.58 eV), confirming the dual Zn atoms accelerate the oxidation of I^- (Fig. S47, ESI†). These outcomes prove that Zn dual atom sites enhance the adsorption/desorption ability and activate polyiodides species, thereby accelerating the redox kinetics of polyiodide conversion.

Conclusions

In summary, we have developed uniformly dispersed Zn diatomic sites in a novel co-pyrolysis method and optimized adsorption-catalysis ability for polyiodides, improving the performance of Zn–I_2 batteries. The atomic structure of Zn_2NC was characterized by high-angle annular dark-field scanning transmission electron microscopy (HAADF-STEM), X-ray absorption near-edge structure (XANES), and Fourier-transformed extended X-ray absorption fine structure (FT-EXAFS) spectra, demonstrating the successful synthesis of Zn dual atom sites. According to the theoretical calculation, the Zn dual atom sites optimize the electronic structure of Zn atoms, which is beneficial for electron filling of iodine molecules under the Fermi level of Zn_2NC to achieve orbital hybridization, thereby enhancing the adsorption/desorption ability of polyiodides, and introducing more active sites promotes the redox kinetics of polyiodides. The batteries with I_2@Zn_2NC cathodes show a high specific capacity of 208 mA h g^{-1} at 0.5C and satisfactory rate performance with a capacity of 105 mA g^{-1} at 50C. More impressively, the cells received the longest cycle of 100 000 cycles at a high current density of 50C and maintained an ultra-low capacity fading rate of 0.0002% per cycle. This work provides a new method for developing high-performance dual atom catalysts, revealing the mechanism of action of dual atom catalysts on polyiodides, and opening up new opportunities for designing high-performance catalysts for state-of-art Zn–I_2 batteries.

Author contributions

C. X. D. designed the experiments and wrote the manuscript. C. X. D. and Y. K. Y. performed the experiments. C. N. M., C. Z. and Z. F. L. carried out the synthesis and analysis. J. J. W. carried out the TEM analysis. J. P. G., J. J. and S. B. Y. carried out the calculation analysis. X. X. and L. Q. M. were in charge of this scientific research project, and the leaders of the actual coordination of the contributions.

Data availability

The data that support the findings of this study are included in the published article and its ESI.† These data are also available from the corresponding authors upon request.

Conflicts of interest

There are no conflicts to declare.

Acknowledgements

This work was supported by the National Natural Science Foundation of China (Grant No. 52127816), the Key Research and Development Program of Hubei (2022BAA027), the National Key Research and Development Program of China (Grant No. 2020YFA0715000), the National Energy-Saving and Low-Carbon Materials Production and Application Demonstration Platform Program (TC220H06N) and the authors would like to acknowledge the Synchrotron Light Research Institute (Public Organization), SLRI, for the provision of beamtime. We also appreciate Dr Suttipong Wannapaiboon and the staff of beamline 1.1W for their assistance.

Notes and references

1 C. Yang, J. Chen, X. Ji, T. P. Pollard, X. Lü, C.-J. Sun, S. Hou, Q. Liu, C. Liu, T. Qing, Y. Wang, O. Borodin, Y. Ren, K. Xu and C. Wang, *Nature*, 2019, **569**, 245–250.
2 S. Ma, J. Zhao, Q. Gao, C. Song, H. Xiao, F. Li and G. Li, *Angew. Chem., Int. Ed.*, 2023, e202315564.
3 C. Dai, L. Hu, X. Jin, Y. Zhao and L. Qu, *Small*, 2021, **17**, 2008043.
4 G. Wang, M. Zhu, G. Chen, Z. Qu, B. Kohn, U. Scheler, X. Chu, Y. Fu, O. G. Schmidt and X. Feng, *Adv. Mater.*, 2022, **34**, 2201957.
5 L. Ma, Y. Ying, S. Chen, Z. Huang, X. Li, H. Huang and C. Zhi, *Angew. Chem., Int. Ed.*, 2021, **60**, 3791–3798.
6 J. Ma, M. Liu, Y. He and J. Zhang, *Angew. Chem., Int. Ed.*, 2021, **60**, 12636–12647.
7 J. Du, Y. Zhao, X. Chu, G. Wang, C. Neumann, H. Xu, X. Li, M. Löffler, Q. Lu, J. Zhang, D. Li, J. Zou, D. Mikhailova, A. Turchanin, X. Feng and M. Yu, *Adv. Mater.*, 2024, **36**, 2313621.
8 H. Chen, X. Li, K. Fang, H. Wang, J. Ning and Y. Hu, *Adv. Energy Mater.*, 2023, **13**, 2302187.
9 D. Lin and Y. Li, *Adv. Mater.*, 2022, **34**, 2108856.
10 H. Yang, Y. Qiao, Z. Chang, H. Deng, P. He and H. Zhou, *Adv. Mater.*, 2020, **32**, 2004240.
11 S. Lian, Z. Cai, M. Yan, C. Sun, N. Chai, B. Zhang, K. Yu, M. Xu, J. Zhu, X. Pan, Y. Dai, J. Huang, B. Mai, L. Qin, W. Shi, Q. Xin, X. Chen, K. Fu, Q. An, Q. Yu, L. Zhou, W. Luo, K. Zhao, X. Wang and L. Mai, *Angew. Chem., Int. Ed.*, 2024, e202406292.
12 S. Lv, T. Fang, Z. Ding, Y. Wang, H. Jiang, C. Wei, D. Zhou, X. Tang and X. Liu, *ACS Nano*, 2022, **16**, 20389–20399.
13 W. Gao, S. Cheng, Y. Zhang, E. Xie and J. Fu, *Adv. Funct. Mater.*, 2023, **33**, 2211979.
14 X. Li, N. Li, Z. Huang, Z. Chen, G. Liang, Q. Yang, M. Li, Y. Zhao, L. Ma, B. Dong, Q. Huang, J. Fan and C. Zhi, *Adv. Mater.*, 2021, **33**, 2006897.
15 P. Lin, G. Chen, Y. Kang, M. Zhang, J. Yang, Z. Lv, Y. Yang and J. Zhao, *ACS Nano*, 2023, **17**, 15492–15503.
16 J. Yang, T. Xiao, T. Xiao, J. Li, Z. Yu, K. Liu, P. Yang and H. J. Fan, *Adv. Mater.*, 2024, 2313610.

17 W. Du, L. Miao, Z. Song, X. Zheng, C. Hu, Y. Lv, L. Gan and M. Liu, *Chem. Eng. J.*, 2024, **484**, 149535.
18 K. Lu, Z. Hu, J. Ma, H. Ma, L. Dai and J. Zhang, *Nat. Commun.*, 2017, **8**, 527.
19 X. Yang, H. Fan, F. Hu, S. Chen, K. Yan and L. Ma, *Nano-Micro Lett.*, 2023, **15**, 126.
20 F. Wang, J. Tseng, Z. Liu, P. Zhang, G. Wang, G. Chen, W. Wu, M. Yu, Y. Wu and X. Feng, *Adv. Mater.*, 2020, **32**, 2000287.
21 H. X. Dang, A. J. Sellathurai and D. P. J. Barz, *Energy Storage Mater.*, 2023, **55**, 680–690.
22 Y. Ji, J. Xie, Z. Shen, Y. Liu, Z. Wen, L. Luo and G. Hong, *Adv. Funct. Mater.*, 2023, **33**, 2210043.
23 Y. Kang, G. Chen, H. Hua, M. Zhang, J. Yang, P. Lin, H. Yang, Z. Lv, Q. Wu, J. Zhao and Y. Yang, *Angew. Chem., Int. Ed.*, 2023, **62**, e202300418.
24 K. Zhang, Q. Yu, J. Sun, Z. Tie and Z. Jin, *Adv. Mater.*, 2023, 2309838.
25 S. Zhang, J. Hao, H. Li, P. Zhang, Z. Yin, Y. Li, B. Zhang, Z. Lin and S. Qiao, *Adv. Mater.*, 2022, **34**, 2201716.
26 K. Wang, H. Li, Z. Xu, Y. Liu, M. Ge, H. Wang, H. Zhang, Y. Lu, J. Liu, Y. Zhang, Y. Tang and S. Chen, *Adv. Energy Mater.*, 2024, **14**, 2304110.
27 H. Zhao, D. Yin, Y. Qin, X. Cui, J. Feng, Y. Zhang, L. Zhao, N. Gao, M. Cui, C. Xiao, G. Feng, Y. Su, K. Xi and S. Ding, *J. Am. Chem. Soc.*, 2024, **146**(10), 6744.
28 J.-L. Yang, H.-H. Liu, X.-X. Zhao, X.-Y. Zhang, K.-Y. Zhang, M.-Y. Ma, Z.-Y. Gu, J.-M. Cao and X.-L. Wu, *J. Am. Chem. Soc.*, 2024, **146**(10), 6628.
29 M. Liu, Q. Chen, X. Cao, D. Tan, J. Ma and J. Zhang, *J. Am. Chem. Soc.*, 2022, **144**, 21683–21691.
30 L. Chai, X. Wang, Y. Hu, X. Li, S. Huang, J. Pan, J. Qian and X. Sun, *Adv. Sci.*, 2022, **9**, 2105063.
31 M. Chen, W. Zhu, H. Guo, Z. Tian, L. Zhang, J. Wang, T. Liu, F. Lai and J. Huang, *Energy Storage Mater.*, 2023, **59**, 102760.
32 J. He, Y. Mu, B. Wu, F. Wu, R. Liao, H. Li, T. Zhao and L. Zeng, *Energy Environ. Sci.*, 2024, **17**, 323–331.
33 Z. Li, W. Cao, T. Hu, Y. Hu, R. Zhang, H. Cui, F. Mo, C. Liu, C. Zhi and G. Liang, *Angew. Chem., Int. Ed.*, 2024, **63**, e202317652.
34 W. Liu, P. Liu, Y. Lyu, J. Wen, R. Hao, J. Zheng, K. Liu, Y.-J. Li and S. Wang, *ACS Appl. Mater. Interfaces*, 2022, **14**, 8955–8962.
35 T. Liu, H. Wang, C. Lei, Y. Mao, H. Wang, X. He and X. Liang, *Energy Storage Mater.*, 2022, **53**, 544–551.
36 X. Liu, H. Wang, J. Zhong, Z. Ma, W. Liu, R. Zhang, M. Li, F. Jiang and L. Kang, *J. Energy Storage*, 2024, **84**, 110765.
37 Y. Du, R. Kang, H. Jin, W. Zhou, W. Zhang, H. Wang, J. Qin, J. Wan, G. Chen and J. Zhang, *Adv. Funct. Mater.*, 2023, 2304811.
38 Y. Wang, X. Jin, J. Xiong, Q. Zhu, Q. Li, R. Wang, J. Li, Y. Fan, Y. Zhao and X. Sun, *Adv. Mater.*, 2024, 2404093.
39 F. Yang, J. Long, J. A. Yuwono, H. Fei, Y. Fan, P. Li, J. Zou, J. Hao, S. Liu, G. Liang, Y. Lyu, X. Zheng, S. Zhao, K. Davey and Z. Guo, *Energy Environ. Sci.*, 2023, **16**, 4630–4640.
40 L. Ma, G. Zhu, Z. Wang, A. Zhu, K. Wu, B. Peng, J. Xu, D. Wang and Z. Jin, *Nano Lett.*, 2023, **23**, 5272–5280.
41 J. Jiao, R. Lin, S. Liu, W.-C. Cheong, C. Zhang, Z. Chen, Y. Pan, J. Tang, K. Wu, S.-F. Hung, H. M. Chen, L. Zheng, Q. Lu, X. Yang, B. Xu, H. Xiao, J. Li, D. Wang, Q. Peng, C. Chen and Y. Li, *Nat. Chem.*, 2019, **11**, 222–228.
42 L. Zhang, J. M. T. A. Fischer, Y. Jia, X. Yan, W. Xu, X. Wang, J. Chen, D. Yang, H. Liu, L. Zhuang, M. Hankel, D. J. Searles, K. Huang, S. Feng, C. L. Brown and X. Yao, *J. Am. Chem. Soc.*, 2018, **140**, 10757–10763.
43 Z. Lu, B. Wang, Y. Hu, W. Liu, Y. Zhao, R. Yang, Z. Li, J. Luo, B. Chi, Z. Jiang, M. Li, S. Mu, S. Liao, J. Zhang and X. Sun, *Angew. Chem.*, 2019, **131**, 2648–2652.
44 J. Wang, Z. Huang, W. Liu, C. Chang, H. Tang, Z. Li, W. Chen, C. Jia, T. Yao, S. Wei, Y. Wu and Y. Li, *J. Am. Chem. Soc.*, 2017, **139**, 17281–17284.